

# NAVAL POSTGRADUATE SCHOOL MONTEREY, CALIFORNIA



## THESIS

**ATMOSPHERIC PROPAGATION SIMULATIONS  
AND BOEING'S HIGH AVERAGE POWER  
FREE ELECTRON LASER**

**by**

**Luis Ramos**

**December 1995**

**Thesis Advisor:**

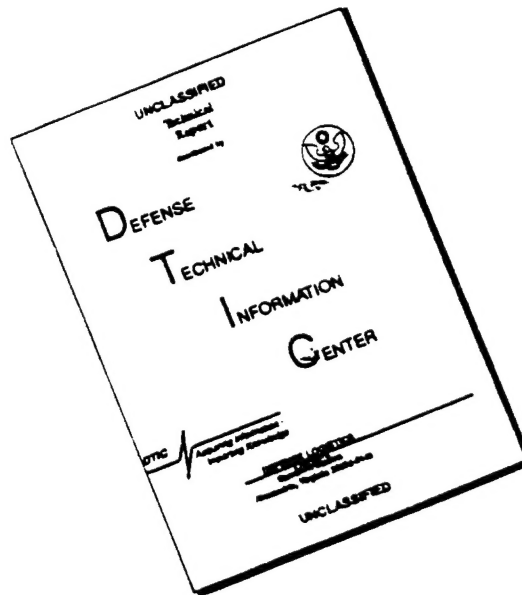
**William B. Colson**

**Approved for public release; distribution is unlimited.**

**19960329 096**

**UNCLASSIFIED**

# DISCLAIMER NOTICE



THIS DOCUMENT IS BEST QUALITY AVAILABLE. THE COPY FURNISHED TO DTIC CONTAINED A SIGNIFICANT NUMBER OF PAGES WHICH DO NOT REPRODUCE LEGIBLY.

REPORT DOCUMENTATION PAGE			Form Approved OMB No. 0704-0188	
Public reporting burden for this collection of information is estimated to average 1 hour per response, including the time for reviewing instruction, searching existing data sources, gathering and maintaining the data needed, and completing and reviewing the collection of information. Send comments regarding this burden estimate or any other aspect of this collection of information, including suggestions for reducing this burden, to Washington Headquarters Services, Directorate for Information Operations and Reports, 1215 Jefferson Davis Highway, Suite 1204, Arlington, VA 22202-4302, and to the Office of Management and Budget, Paperwork Reduction Project (0704-0188) Washington DC 20503.				
1. AGENCY USE ONLY (Leave blank)		2. REPORT DATE December 1995		3. REPORT TYPE AND DATES COVERED Master's Thesis
4. TITLE AND SUBTITLE ATMOSPHERIC PROPAGATION SIMULATIONS AND BOEING'S HIGH AVERAGE POWER FREE ELECTRON LASER			5. FUNDING NUMBERS	
6. AUTHOR(S) Luis Ramos				
7. PERFORMING ORGANIZATION NAME(S) AND ADDRESS(ES) Naval Postgraduate School Monterey CA 93943-5000			8. PERFORMING ORGANIZATION REPORT NUMBER	
9. SPONSORING/MONITORING AGENCY NAME(S) AND ADDRESS(ES)			10. SPONSORING/MONITORING AGENCY REPORT NUMBER	
11. SUPPLEMENTARY NOTES The views expressed in this thesis are those of the author and do not reflect the official policy or position of the Department of Defense or the U.S. Government.				
12a. DISTRIBUTION/AVAILABILITY STATEMENT Approved for public release; distribution is unlimited.			12b. DISTRIBUTION CODE	
13. ABSTRACT (maximum 200 words)  The development of a high average power FEL for military applications, whether shipboard or not, represents a significant advancement in technology over present weapons systems design. The FEL has significant advantages over conventional kinetic systems and other classical high-energy laser systems. The rapid response, wavelength tunability, and infinite magazine make the FEL a highly desirable shipboard weapon system.  The initial part of this thesis examines the advantages of a FEL over a conventional kinetic weapon. Section II explores the atmospheric phenomenon that affects the propagation of a laser beam enroute to its target. Section III presents the Boeing FEL proposal followed by the theory of the FEL. Lastly, in Sections V, VI, simulations are conducted to analyze the FEL's feasibility.				
14. SUBJECT TERMS Atmospheric Propagation Simulations, Free Election Lasers			15. NUMBER OF PAGES 64	
			16. PRICE CODE	
17. SECURITY CLASSIFICATION OF REPORT Unclassified	18. SECURITY CLASSIFICATION OF THIS PAGE Unclassified	19. SECURITY CLASSIFICATION OF ABSTRACT Unclassified	20. LIMITATION OF ABSTRACT UL	



Approved for public release: distribution is unlimited.

**ATMOSPHERIC PROPAGATION SIMULATIONS AND  
BOEING'S HIGH AVERAGE POWER FREE ELECTRON LASER**

**L. Ramos**

Lieutenant, United States Navy

B. S., United States Naval Academy, 1989

Submitted in partial fulfillment of the  
requirements for the degree of

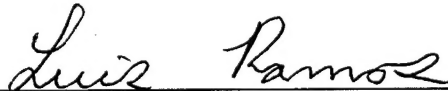
**MASTER OF SCIENCE IN APPLIED PHYSICS**

from the

**NAVAL POSTGRADUATE SCHOOL**

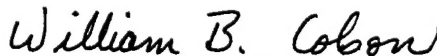
December 1995

Author:

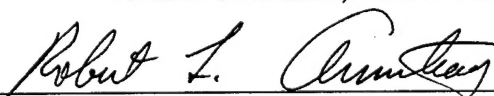


Luis Ramos

Approved by:



William B. Colson, Thesis Advisor



Robert L. Armstead, Second Reader



William B. Colson, Chairman,

Department of Physics



## **ABSTRACT**

The development of a high average power FEL for military applications, whether shipboard or not, represents a significant advancement in technology over present weapon systems design. The FEL has significant advantages over conventional kinetic systems and other classical high-energy laser systems. The rapid response, wavelength tunability, and infinite magazine make the FEL a highly desirable shipboard weapon system.

The initial part of this thesis examines the advantages of a FEL over a conventional kinetic weapon. Section II explores the atmospheric phenomena that affect the propagation of a laser beam enroute to its target. Section III presents the Boeing FEL proposal followed by the theory of the FEL. Lastly, in Sections V and VI, simulations are conducted to analyze the FEL's feasibility.





## TABLE OF CONTENTS

I. INTRODUCTION .....	1
II. LASER BEAM PROPAGATION THROUGH THE ATMOSPHERE .....	5
A. DESCRIPTION OF THE ATMOSPHERE .....	5
B. DIFFRACTION .....	6
C. MODELING A LENS .....	14
D. MODELING TURBULENCE WITH LENSES .....	15
E. THERMAL BLOOMING OVERVIEW .....	21
III. BOEING 1 KILOWATT FEL .....	27
IV. BASIC FEL THEORY .....	29
A. DIMENSIONLESS PARAMETERS .....	30
B. ELECTRON TRAJECTORY .....	31
C. RESONANCE CONDITION .....	34
D. PENDULUM EQUATION .....	35
E. OPTICAL WAVE EQUATION .....	36
F. TRAPPED-PARTICLE INSTABILITY .....	38
G. DESYNCHRONISM .....	40
V. APPLICATION OF BOEING FEL .....	43
VI. CONCLUSION .....	49
LIST OF REFERENCES .....	51
INITIAL DISTRIBUTION LIST .....	53



## **ACKNOWLEDGEMENT**

The author is grateful to Professor Bill Colson and Professor Bob Armstead for their invaluable assistance and guidance throughout this project.

The author also acknowledges the kindness and support of his loving wife Kimberly, and my children Luke and Sophia.



## I. INTRODUCTION

During the Cold War, the "Super Powers" (U.S. & U.S.S.R.) amassed enormous stockpiles of strategic and tactical weapons. Versions of these weapons were distributed to third world allies by both Super Powers. As the cold war dragged on, developed countries such as China and France dramatically increased their missile design capability. Accordingly, these nations began to sell highly advanced missile systems to the highest bidders. With the demise of the cold war, the single Soviet adversary no longer existed. What resulted was the creation of many potential enemies throughout the world. At present, any nation or organization with resolve and financial means can obtain and use modern offensive missile systems. Therefore, we as a nation, as well as our democratic allies, are susceptible to lurking threats from a number of conceivable directions. Political, religious or terrorist groups of various sizes, as well as developing countries struggling to take a stand are all capable of attack.

During Operations Desert Shield and Desert Storm, a major concern of the coalition forces was the possible employment of Chinese-made Silk Worm Anti-Ship Missiles (ASM) by Iran. Fortunately, no ASMs were fired at the coalition forces. In 1987 however, during the Iran-Iraq War, the Iraqis inflicted significant structural damage on the U.S.S. STARK [1] when they successfully fired a French made Exocet ASM. In a similar missile incident during the Falklands War, the Argentinian Navy inflicted catastrophic damage on a British Frigate from an air launched Exocet missile [1]. The world learned two lessons from both these incidents: first, the potential for destruction from an ASM was greater than anticipated; second, vessels at sea are vulnerable to damage because present Anti-Ship Missile Defense (ASMD) technology is far inferior to

ASM technology. Moreover, we came to the alarming realization that the defensive systems utilized by the British and U.S Forces failed to protect the warships from damage. The United States relied heavily on the Close In Weapons System (CIWS) - essentially a 20mm Gatling Gun - and the British relied on the Penguin Gatling Gun.

ASM technology continues to dramatically improve while the predominately 1960's technology of present Anti-Ship Missile Defense System (ASMDS) have only improved in the detection aspects of the system. As an example, the French will soon deploy the Aerospatiale/MBB Supersonic Anti-Ship Missile (ANS) [2] to replace its Exocet missile stockpile. The ANS will be a long range (  $\approx 180$  km) sea skimming missile capable of 10 g terminal deceptive maneuvers ( 1 g is  $9.8\text{m/sec}^2$  ) at speeds in excess of mach 2. As a rule of thumb, ASMD systems need to maneuver at least 3 times more rapidly than the offensive ASM [3]. For a mach 2 missile with 10 g maneuverability this would require an ASMD System that could maneuver at 30 g. If the technology existed to make an ASMD system maneuver at 30 g's, in time it would be incorporated into the ASM design. The endless advancement cycle would always benefit the offensive weapons system. Although the two aforementioned examples focus on the failure of mechanical defensive weapons technology to guard against a potential supersonic ASM, the technology exists to develop a high energy laser system to serve as a "speed-of-light" Anti-Ship Missile Defense System. This laser system would terminate the endless advancement cycle.

The speed-of-light maneuverability of a Shipboard Free-Electron Laser (SFEL) is just one advantage over a kinetic energy defensive weapon system such as a missile. Other characteristics that make a SFEL a superior ASMDS are its relatively endless magazine supply, its tunable wavelength and its high power potential. Section II of this thesis will describe the amount of localized

energy required to destroy a missile and will follow the propagation path of the laser beam back to the SFEL to determine the beam requirements at the laser. Numerical simulation is used to describe the effects of diffraction, turbulence, and thermal blooming on laser beam propagation. Section III will describe Boeing Corporation's 1 Kilowatt Average Power FEL and its potential for use as a SFEL. In Section IV the basic principles of the FEL are described. Lastly, simulations and basic FEL theory are used to evaluate the performance of the Boeing FEL in Section V.





## **II. LASER BEAM PROPAGATION THROUGH THE ATMOSPHERE**

### **A. DESCRIPTION OF THE ATMOSPHERE**

The transmission of laser radiation through the atmosphere results in several processes that alter the nature of the beam. At low average power where the interactions are linear, the effects of scattering and absorption are dominant. At high average power, additional non-linear processes can occur. The performance of a high average power laser operating at sea-level can be severely degraded by these non-linear effects.

As a model for development, our firing platform, the SFEL, and Exocet target are both at sea-level and approximately 14 kilometers apart. The target is in the Line-of-Sight of the SFEL during the entire optical wave propagation. In the absence of an atmosphere the power of the laser beam would be constant in time. The atmosphere, however, produces spatial and temporal fluctuations along the propagation path, resulting in changes in the intensity and power of the beam. This is due to random variations in the atmospheric refractive index along the propagation path. The variations in the atmospheric refractive index primarily result from small temperature variations along the propagation path. To better understand the effect of the refractive index fluctuations, consider the region of high or low refractive index as a lens. In the following section, I will develop the propagating wave using Maxwell's equations and describe the refractive index variations as it applies to the wave equation.

The turbulent atmosphere can then be modeled as a large number of random lenses, varying in size and shape along the propagation path [4]. The turbulence will cause no change in the magnitude of the electromagnetic wave, but a phase change results from the change in velocity of the area of the wave that traverses the lens. The resulting phase variations are not uniform

throughout all points perpendicular to the direction of propagation. These varying perturbations may cause focusing or defocusing effects and local deviations in the direction of wave propagation. Eventually, through interference and diffraction, there are intensity fluctuations and loss of intensity at the missile surface. While the individual effect of a small, single refractive index change over a small distance is minute, the cumulative effect of many refractive index variations can be significant.

## B. DIFFRACTION

To analyze the propagating wave, it is essential to begin with Maxwell's Wave equation [5]. An electromagnetic wave will propagate in the absence of a current density according to

$$\left[ \nabla^2 - \frac{1}{c^2} \frac{\partial^2}{\partial t^2} \right] \vec{A}(\vec{r}, t) = 0 \quad . \quad (1)$$

The first term is the Laplacian  $\nabla^2 = \partial_x^2 + \partial_y^2 + \partial_z^2$ ,  $t$  is the time,  $c$  is the speed of light,  $\vec{r}$  is the vector position, and  $\vec{A}$  is the optical vector potential. The vector potential is complex, containing both phase and amplitude information. The optical electric and magnetic fields can be derived from the vector potential by the following relationships:

$$\vec{E} = - \frac{1}{c} \frac{\partial \vec{A}}{\partial t} \quad , \quad (2)$$

and

$$\vec{B} = \nabla \times \vec{A} \quad . \quad (3)$$

The optical beam propagates in the  $z$  direction along the range,  $R$ , to the target. The beam is assumed to be composed of a single frequency and circularly polarized. The vector potential describing such a beam is

$$\vec{A} = \frac{E}{k}(\sin\Psi, \cos\Psi, 0) \quad , \quad (4)$$

where  $k = 2\pi c/\omega$  is the wave number of the beam, and  $\Psi$  is the phase describing a plane wave,  $\Psi = kz - \omega t + \phi$ . In this expression,  $\omega$  is the angular frequency and  $\phi$  is the optical phase. Since the beam is composed of a single frequency, the variation in the electric field amplitude and phase will be small over the distance of a wavelength,  $\lambda = 2\pi/k$ . Thus,  $\partial E / \partial z \ll kE$ , and  $\partial \phi / \partial z \ll k\phi$ . The variation in the field amplitude and phase in time over a period will also be very small, so that  $\partial E / \partial t \ll \omega E$ , and  $\partial \phi / \partial t \ll \omega \phi$ . Thus, the wave equation contains second-order terms that will be small compared to first or zeroth-order terms. In order to simplify the analysis, these second-order terms are dropped. Substituting in the vector potential, the wave equation then becomes [3],

$$\left[ \frac{\partial^2}{\partial x^2} + \frac{\partial^2}{\partial y^2} + 2ik \left( \frac{\partial}{\partial z} + \frac{1}{c} \frac{\partial}{\partial t} \right) \right] \vec{E} \exp(i\phi) = 0 \quad . \quad (5)$$

The last partial derivatives in  $z$  and  $t$ , describe the propagation of a plane wave. The first partial derivatives in  $x$  and  $y$  describe how the beam changes due to diffraction as it propagates.

Another simplification is to make the terms dimensionless for numerical analysis. A dimensionless time is constructed from  $\tau = ct/R$  where  $\tau$  varies from 0 to 1 over the entire range of travel. It is convenient to follow the wavefront with  $Z = z - ct$ . With this coordinate change,

$$\frac{\partial}{\partial z} = \frac{\partial Z}{\partial z} \frac{\partial}{\partial Z} + \frac{\partial \tau}{\partial z} \frac{\partial}{\partial \tau} = \frac{\partial}{\partial Z} \quad , \quad (6)$$

using  $\partial_z Z = 1$  ( where  $\partial_z \equiv \partial / \partial z$  ) and  $\partial_z \tau = 0$ . Also,

$$\frac{1}{c} \frac{\partial}{\partial t} = \frac{1}{c} \frac{\partial Z}{\partial t} \frac{\partial}{\partial Z} + \frac{1}{c} \frac{\partial \tau}{\partial t} \frac{\partial}{\partial \tau} = \frac{1}{R} \frac{\partial}{\partial \tau} - \frac{\partial}{\partial Z} \quad , \quad (7)$$

using  $\partial_t Z = -c$  ( where  $\partial_t \equiv \partial / \partial t$  ) and  $\partial_t \tau = c / R$ . The plane-wave

operator in the wave equation (5), now becomes

$$\frac{\partial}{\partial z} + \frac{1}{c} \frac{\partial}{\partial t} = \frac{\partial}{\partial Z} + \frac{1}{R} \frac{\partial}{\partial \tau} - \frac{\partial}{\partial Z} = \frac{1}{R} \frac{\partial}{\partial \tau} \quad (8)$$

The wave equation becomes

$$\left[ \frac{\partial^2}{\partial x^2} + \frac{\partial^2}{\partial y^2} + 2ik \frac{1}{R} \frac{\partial}{\partial \tau} \right] \vec{E} \exp(i\phi) = 0 \quad , \quad (9)$$

and is known as the parabolic wave equation. The parabolic wave equation relates the transverse size of the beam to its propagation distance  $R$ , and can be rewritten as

$$\left[ \frac{-iR}{2k} \nabla_{\perp}^2 + \frac{\partial}{\partial \tau} \right] \vec{E} \exp(i\phi) = 0 \quad , \quad (10)$$

where the  $\nabla_{\perp}^2$  operator is the transverse Laplacian,  $\nabla_{\perp}^2 = \partial_x^2 + \partial_y^2$ . If the transverse variables,  $x$  and  $y$ , are made dimensionless through  $x \rightarrow x\sqrt{k/2R}$ , and  $y \rightarrow y\sqrt{k/2R}$ , Equation (10) becomes

$$\frac{\partial a}{\partial \tau} = \frac{i}{4} \nabla_{\perp}^2 a \quad , \quad (11)$$

where the complex, dimensionless, optical field is  $a = |a| \exp(i\phi)$ . Since (11) is linear in the electric field,  $E \propto a$ , a simple scale factor can make the field dimensionless and normalized to unity. Equation (11) describes how the dimensionless complex field,  $a(x,y,\tau)$ , evolves in the dimensionless time,  $\tau$ , and the dimensionless transverse coordinates  $x$  and  $y$ .

The complex field may also be written as the sum of its real and imaginary components  $a = a_r + ia_i = |a| \exp(i\phi)$ . Equation (11) can thus be separated into real and imaginary parts,

$$\frac{\partial a_r}{\partial \tau} = -\frac{1}{4} \nabla_{\perp}^2 a_i \quad , \quad (12)$$

$$\frac{\partial a_i}{\partial \tau} = \frac{1}{4} \nabla_{\perp}^2 a_r \quad . \quad (13)$$

Equations (12) and (13) describe the motion of the laser beam as it propagates to the target and include diffraction of the optical wave. The complex field  $a$  evolves in time  $\tau$  along the range  $R$ . As  $\tau = 0 \rightarrow 1$ , the wavefront evolves along the range to the target. A wavefront of large size,  $\Delta x, \Delta y \rightarrow \infty$ , a plane wave, will not be affected by diffraction since the divergence of  $a$  becomes small. However, if the structure size is smaller, it will be affected by diffraction. Specifically, if  $\Delta x \approx \Delta y$  characterizes the spatial extent of the beam in cross section and  $\Delta\tau = 1$  over the full range of propagation, then diffraction is important when  $\Delta\tau / (4\Delta x^2) \approx 1$ . In summary, a large wave front with structure size  $\Delta x, \Delta y \gg 1$  is not seriously affected by diffraction compared to a small wavefront with structure size  $\Delta x, \Delta y \leq 1$ . Equations (12) and (13) are linear, complex equations with symmetry in the  $x$  and  $y$  directions.

Equations (12) and (13) can be solved numerically and the complex field determined for any  $x$  and  $y$  as the beam traverses  $\tau$ . The propagation simulation code [3] uses two-dimensional (2-D) arrays for the real ( $ar[x][y]$ ) and imaginary ( $ai[x][y]$ ) parts of the field. The program then steps these arrays along the dimensionless time,  $\tau = 0$  to 1. At each step, the program calculates the new part of the field, real and imaginary, using the previous parts of the field. The Laplacian is calculated by determining the field difference between the  $x$  and  $y$  points prior to and after each time step. Every 2-D array has square dimensions, and each address assignment contains a floating point number. The mathematical derivation of this process is as follows:

$$a[x][y] = ar[x][y] + iai[x][y] \quad . \quad (14)$$

In this derivation process  $a$  refers to either  $ar$  or  $ai$ . Evaluating to the right gives

$$\frac{\partial a}{\partial x} = \frac{a[x+1][y] - a[x][y]}{dx} \quad , \quad (15)$$

and evaluating to the left gives

$$\frac{\partial a}{\partial x} = \frac{a[x][y] - a[x-1][y]}{dx} \quad (16)$$

To evaluate  $\partial^2 a / \partial x^2$ , it is important that both right and left partial derivatives be used to maintain the symmetry of Equation (11) and to balance between adjacent array locations. Thus,

$$\frac{\partial}{\partial x} \left( \frac{\partial a}{\partial x} \right) = \frac{1}{dx} \left[ \frac{a[x+1][y] - a[x][y]}{dx} - \frac{a[x][y] - a[x-1][y]}{dx} \right], \quad (17)$$

$$\frac{\partial^2 a}{\partial x^2} = \frac{a[x+1][y] + a[x-1][y] - 2a[x][y]}{dx^2} \quad (18)$$

The y component equations are similarly derived. Equation (11) can be written numerically as

$$dar[x][y] = -\frac{d\tau}{4} \left[ \frac{\partial^2}{\partial x^2} + \frac{\partial^2}{\partial y^2} \right] ai[x][y], \quad (19)$$

and

$$dai[x][y] = \frac{d\tau}{4} \left[ \frac{\partial^2}{\partial x^2} + \frac{\partial^2}{\partial y^2} \right] ar[x][y] \quad (20)$$

Where  $dar$  and  $dai$  are respectively, the dimensionless time derivative of the real and imaginary parts of the field. The numerical coefficient  $C$  in the algorithm is  $d\tau/(4dx^2)$ . It serves as the propagation front diffraction operator, where the time-step is  $d\tau = 1/nt$ , and  $nt$  is the total number of time steps over the range  $0 \rightarrow 1$ . Additionally, the finite grid size is  $dx = dy = W/nx$ , which is the quotient of the transverse window width ( $W$ ) and the number of bin elements ( $nx$ ) in the x and y directions. Substituting Equation (18) and its y counterpart into Equations (19) and (20) yields a numerical solution to the wave equation. Furthermore, as explained in the analytical derivation, a wavefront will be affected by diffraction if  $C \approx 1$ .

An analytical solution to the optical wave equation gives the following relation between the dimensionless Rayleigh length  $z_0$  [3], the mode waist radius  $w_0$ , and the wavelength  $\lambda$ :

$$z_0 = \frac{\pi w_0^2}{\lambda R} \quad . \quad (21)$$

The Rayleigh length gives the characteristic distance over which the beam waist will double in transverse area along its propagation path [6].

Figure 1 describes a typical Gaussian optical mode in a resonator with spherical mirrors. This is the output of the simulation code for  $z_0 = 0.5$  and the location of the mode waist in the middle of the range  $\tau_w = 0.5$ . Where  $\tau_w$  is the dimensionless time which specifies the mode waist location. At  $\tau_w$  the laser beam spreads by diffraction as it moves beyond  $\tau_w$ . The top left window depicts the side view of a beam profile with the peak dimensionless optical field shown in brackets. The intensity scale of the windows is such that regions where no light is present are dark and the bright regions indicate where light has propagated. The contour lines show where the optical field amplitude is 50% of the maximum. The vertical axis is the dimensionless  $x$  direction and the horizontal axis is the dimensionless time variable  $\tau = 0 \rightarrow 1$ . The wavefront initially focuses at  $\tau = 0.5$  and then it spreads. As the beam passes the mode waist location, it spreads along  $\tau$ . The top right window shows the peak dimensionless optical amplitude at the end of the simulation  $\tau = 1$ . The bottom window shows the peak dimensionless optical field from a top view perspective. Observe how the optical field is symmetric about the  $x$  and  $y$  directions from both the top and side views. This results from having no inhomogeneities along the propagation path. The data on the right lists the value of the numerical coefficient  $C$ , the number of time steps  $nt$ , the number of bin elements  $nx$ , and the corresponding error in the calculation. The error computation is given by the ratio of the change in energy to the energy  $dE/E$  over consecutive bins.

Specifically, this relationship is given by:

$$E = \sum_{x,y} a^2[x][y] \quad , \quad (22)$$

and

$$\frac{dE}{E} = \frac{(E_f - E_0)}{E_0} \quad , \quad (23)$$

where  $E_f$  and  $E_0$  are respectively, the final and initial energies. Below the error calculation is an optical field intensity bar scale. The scale shows the magnitude of the dimensionless optical field amplitude.

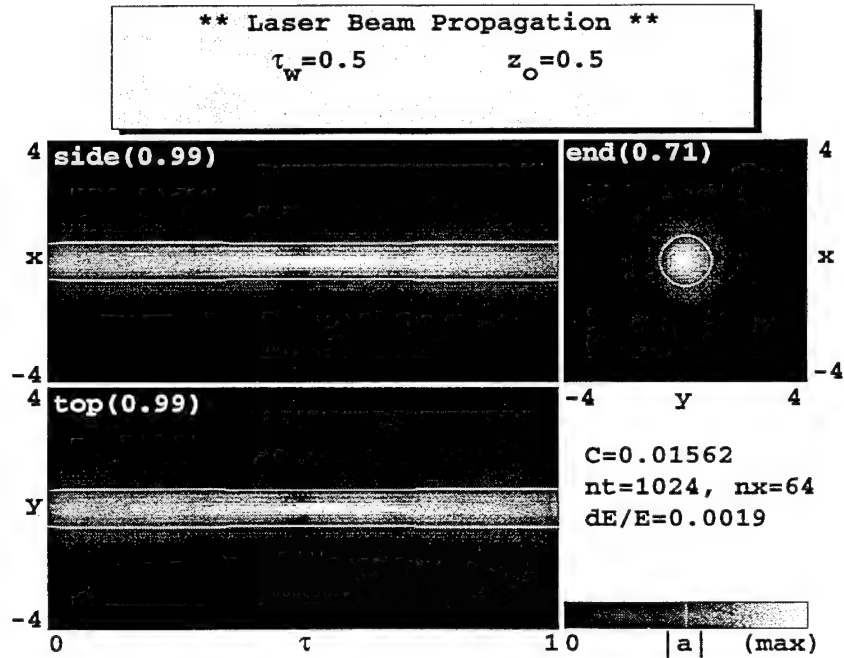


Figure 1. Propagation path with no inhomogeneities.

An alternate method of solving Equation (11) is by implementing a Fast Fourier Transform (FFT) [6]. The first step in this process is to show that

$$a(\tau) = \exp\left[\frac{i\tau\nabla_{\perp}^2}{4}\right] a(0) \quad , \quad (24)$$



is a solution to Equation (11). Thus, substituting Equation (24) into (11) yields:

$$\frac{da}{d\tau} \equiv \dot{a} = a(0) \frac{\partial}{\partial \tau} \left[ \exp \left( \frac{i\tau \nabla_{\perp}^2}{4} \right) \right] = \frac{i\nabla_{\perp}^2}{4} \left[ a(0) \exp \left( \frac{i\tau \nabla_{\perp}^2}{4} \right) \right] = \frac{i\nabla_{\perp}^2}{4} a(\tau) \quad , \quad (25)$$

which is Equation (11). Therefore, Equation (24) is a solution to the dimensionless, parabolic wave equation. Translating Equation (24) by a dimensionless time step  $\Delta\tau$  results in:

$$a(\tau + \Delta\tau) = \exp \left[ \frac{i\Delta\tau \nabla_{\perp}^2}{4} \right] a(\tau) \quad . \quad (26)$$

An exact numerical solution can then be derived by applying a FFT to Equation (24) and multiplying it by the diffraction operator, and then taking the inverse FFT. Without tracing through the mathematics, the procedure is:

$$a(\tau + \Delta\tau) = FFT^{-1} \left[ \exp \left[ \frac{-i\Delta\tau k^2}{4} \right] FFT(a(\tau)) \right] \quad . \quad (27)$$

Since this solution is exact, and  $\Delta\tau$  need not be infinitesimal, no numerical errors are introduced into the propagation of the wavefront.

Figure 2 illustrates a Gaussian optical mode in a resonator with spherical mirrors utilizing the FFT technique. This is the output for  $z_0 = 0.2$  and the mode waist is located at the end of the range  $\tau_w = 1.0$ . As expected no errors propagated through the calculation. This can be seen from  $dE/E = 0$ . In this simulation the beam focuses at the end of the propagation path. The diffraction operator forces the beam to focus at the beam waist location  $\tau_w$ . This is of particular interest to a SFEL since the maximum field intensity should be concentrated on the target. The following sections explore how the atmosphere affects beam quality.

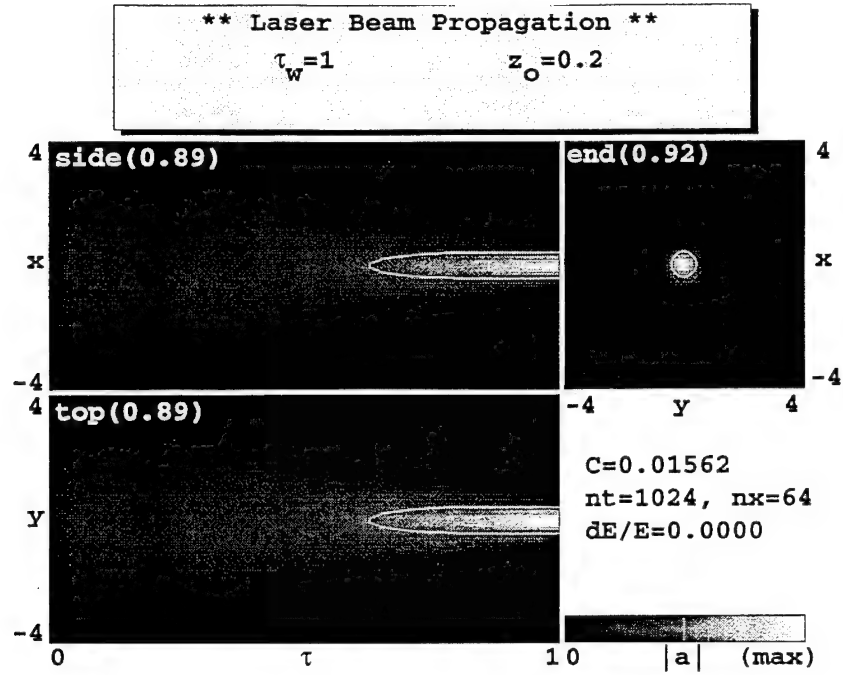


Figure 2. Propagation simulation incorporating FFT technique.

### C. MODELING A LENS

As a laser beam travels through a volume element in the atmosphere, or in any medium, its propagation is affected by the medium's index of refraction  $n = c/v$ . Where  $c$  is the speed of light in free space and  $v$  is the speed of light in the medium. The non-uniform density of the volume element results in a changing index of refraction across the beam cross-section. The varying index of refraction along the transverse axis of the beam is similar to the change in the refractive power across a lens depending on the thickness of the lens [3]. A lens will have varying affects on distinct segments of the beam. The overall effect is to induce a phase shift across the wavefront which is dependent on the thickness of the lens it passes through. Specifically, this phase shift can be represented by the following relation:

$$a_{out} = a_{in} \exp(i\Delta\phi) \quad . \quad (28)$$

Where  $a_{in}$  is the complex field entering a path segment of length  $\Delta z$ ,  $\Delta\phi$  is the phase shift resulting from the  $\Delta z$ , and  $a_{out}$  is the exiting complex field. Comparing a wavelength of a ray which passes through the center of the lens with one which passes through a portion of the lens a distance  $r$  from the center, a phase shift will be introduced between the two rays according to the relation:

$$\Delta\phi = \frac{-2\pi r^2}{\lambda r_c} \quad (29)$$

Where  $\Delta\phi$  is the dimensionless phase shift, and  $r_c$  is the radius of curvature of the lens. The propagation code uses the operator in Equation (28) to model the effect of a lens on the propagation of the beam.

As an example, Figure 3 illustrates placing a lens at  $\tau = 0.3$  with a strength of  $d\phi = 3$ . Where  $d\phi$  is the phase delay (or advance) introduced by the presence of a lens. The portion of the beam passing through the center of the lens is impeded more than at the edges. The effect of the lens is to cause strong focusing of the beam at  $\tau = 0.6$ . At  $\tau = 1$ , the beam is beyond its focal point and spreads out again. Additionally, this simulation incorporates a Fast Fourier Transform technique to propagate the wavefront. Figure 4 simulates having the lens in the same position but with a lens strength of  $d\phi = -3$ . In this case the portion of the beam passing through the center of the lens is impeded less than the edges and the lens defocuses the beam.

#### D. MODELING TURBULENCE WITH LENSES

Consider the SFEL model as the transmitter and a stationary platform as the target within the line-of-sight (LOS) of the SFEL. When the SFEL is fired in a continuous wave mode at the platform target, the intensity of the intervening turbulence the beam wave encounters as it propagates towards the target varies in a diurnal cycle [4]. Atmospheric turbulence effects are smaller at night

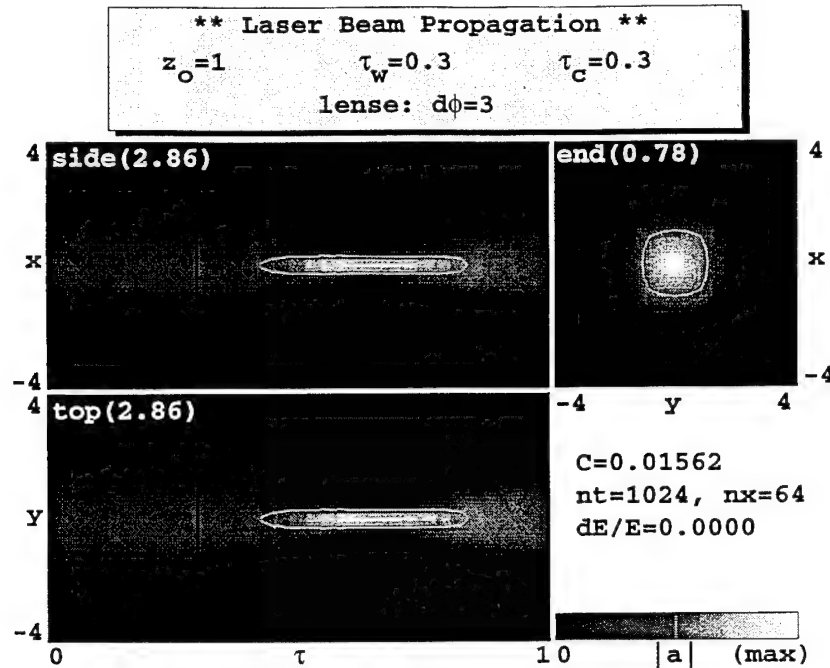


Figure 3. Propagation path with a converging lens.

and in the early morning hours than during the mid-day hours when solar heating of the earth becomes significant enough to initiate convective heating currents [7]. The convective heating current or instability generates temperature fluctuations as a function of height. That is, the sun-heated surface materials warm a thin layer of the air above it. Air parcels from the layer, displaced upward, are warmer, less dense, and more buoyant than the ambient air. The mixing of these hot air parcels with the cool descending air parcels produces isobaric temperature irregularities which cause fluctuations in the index of refraction. The measurement of these temperature fluctuations provides a measure of local turbulence [8]. If one considers turbulence as varying indices of refraction through a small, isobaric, volume element, then turbulence can be modeled as a series of random lenses with varying indices of refraction.

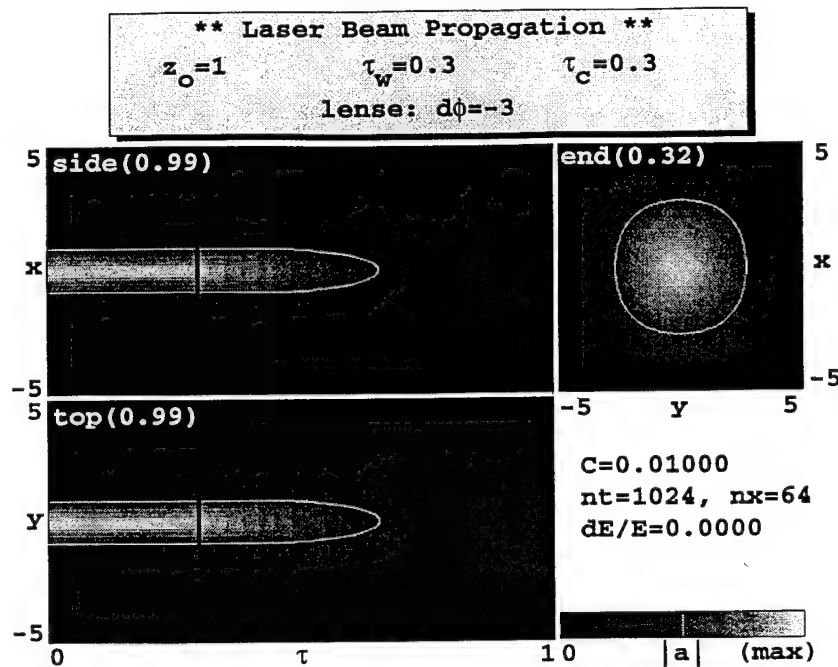


Figure 4. Propagation path with a diverging lens.

The simulation code uses a series of random lens' superimposed on each other to represent propagation through a turbulent atmosphere. The index of refraction is directly coupled to variations in temperature by the relation  $n - 1 \approx -10^{-6} dT$  [3]. In this approximation,  $dT$  is an incremental change in temperature ( $^{\circ}C$ ) within the isobaric volume element of air. As an example, a temperature increase within the isobaric volume element of  $dT \approx 1^{\circ}C$  will decrease the air density in the region, and therefore, decrease the index of refraction by  $n - 1 \approx -10^{-6}$ . Conversely, a temperature decrease of  $dT \approx -1^{\circ}C$  will increase the air density and the index of refraction by  $n - 1 \approx 10^{-6}$ .

The index of refraction  $n$  is related to a dimensionless spatial increment  $dz$  through the following derivation. By definition  $n$  is the quotient of light speed in vacuum and light speed in a medium. Specifically, this is given by:

$$n = \frac{c}{v} \quad . \quad (30)$$

Differentiating  $n$  in terms of  $v$  and regrouping the terms gives

$$dn = \frac{-c}{v^2} dv \quad . \quad (31)$$

By approximating that  $v$  is nearly equivalent to  $c$ , Equation (31) simplifies to

$$dn \approx \frac{-dv}{c} \quad . \quad (32)$$

This difference in index of refraction gives the light speed difference  $dv$ , and the speed difference also results in an optical phase difference

$$d\phi = \frac{2\pi dv dz}{c\lambda} \quad , \quad (33)$$

over the random element of path  $dz$ . Now, recalling that  $dn = n - 1 \approx -10^{-6} dT$ , then the index of refraction can be incorporated into the propagation code by the approximation:

$$d\phi \approx 2\pi \times 10^{-6} \left[ \frac{dz}{\lambda} \right] dT \quad . \quad (34)$$

In general, beam irradiance deposited on a target is dependent on the turbulence encountered along the propagation path.

A phase screen operator of the form  $\exp(id\phi)$ , similar to the lens operator of Section C, represents the effect of different columns of volume elements with varied indices of refraction. Randomly applying phase screen operators to segments of the propagation path, results in the simulation of a random, turbulent propagation path. Each component of the phase screen has a random  $\vec{k}$  vector. The amplitude of the random  $\vec{k}$  is given by the probability distribution  $P(k) \propto k^{-5/6}$ [3]. An exponential distribution of characteristic wavenumbers may also be used to determine the Fourier component amplitude. The direction angle  $\chi$  is used to determine a random wavenumber in the  $x$  and

y directions:  $k_x = k \cos(2\pi\chi)$  and  $k_y = k \sin(2\pi\chi)$ . Each phase screen is constructed from many Fourier components. A single component of the numerical phase screen operator is  $\Delta\phi \sin(k_x x + k_y y + 2\pi\chi_2)$ , where  $\chi_2$  is another random number between 0 and 1. Each component is a lens with a random sinusoidal surface randomly oriented in each phase screen to represent the random turbulence over the propagation path. The end views of Figure 5 and 6 illustrate how significantly the wavelength affects beam scintillation. A characteristic wave number of  $k_c = 3$  results in fewer beam spots and thus a tighter beam concentration on the target than Figure 6 which has  $k_c = 7$  and all other parameters equal. This is in general agreement with the experimental and simulation results given by Gebhart [9].

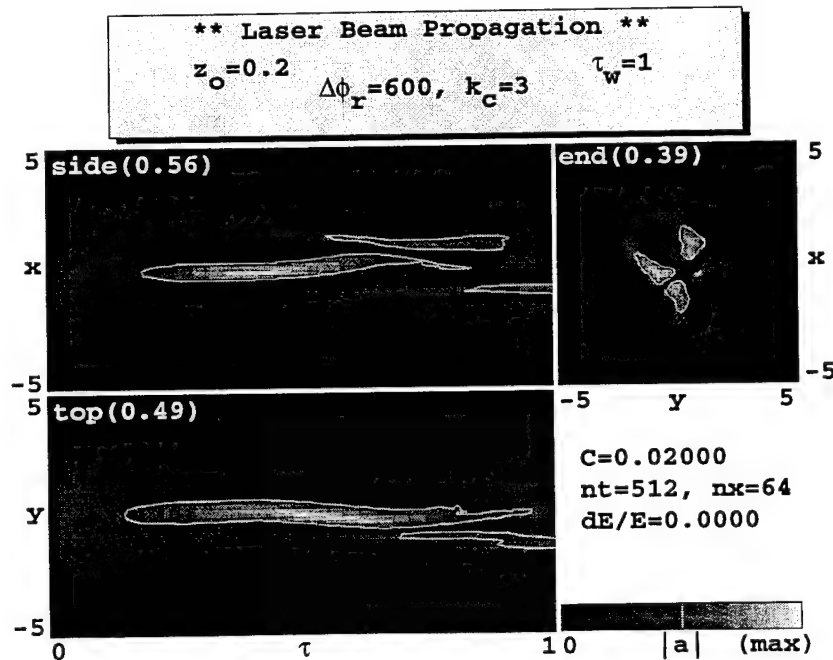


Figure 5. Wavelength affects on beam scintillation.

An outcome of the perturbations along the propagation path is that the beam phase is altered and its energy is redirected. Each beam spot can be

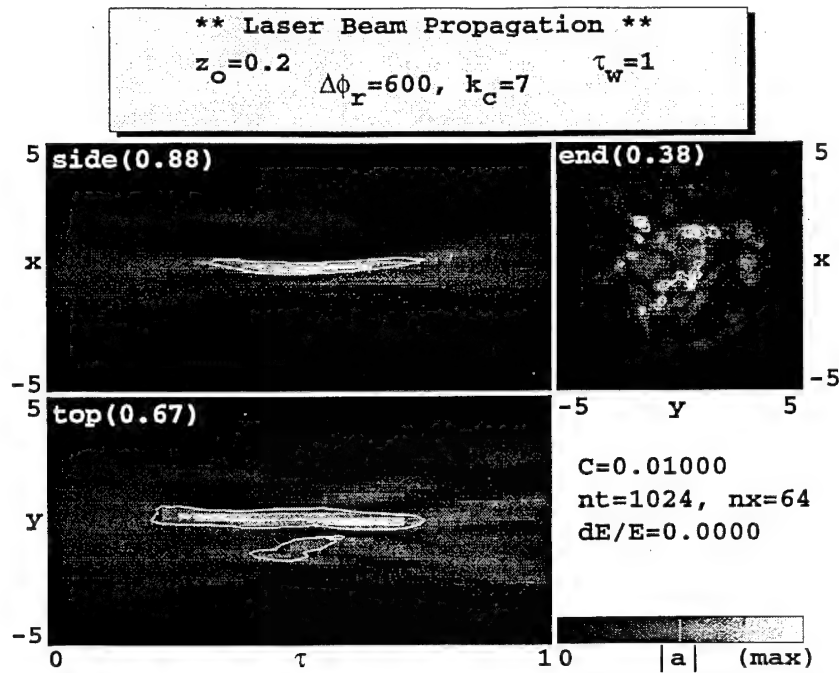


Figure 6. Variation of characteristic wave number.

approximately the size of the transmitter's diffraction limit [7]. In the presence of strong turbulence, the beam wave breaks up into groups of beam spots. Thus, the phase distortions could become so large that beam focusing would be impossible. This is of concern to the SFEL model since it is crucial to have the beam focused on its target. A comparison of Figures 2 and 6 reveals how detrimental turbulence can be on beam quality. In Figure 2 the beam propagated through a homogeneous atmosphere and focused on the platform target. The simulation in Figure 6 maintained the same parameters but added an inhomogeneous propagation path. The nonhomogeneity, or turbulence, is represented by the total phase variable  $\Delta\phi_r = 600$ . The larger the value of the phase, the more turbulence encountered by the propagating beam. Additionally, a characteristic wave number  $k_c = 7$  was added. The end view reveals a dispersion of spots concentrated over a larger area when compared



to the end view of Figure 2. Thus, the turbulent medium makes it difficult to focus the beam's energy on the target.

## **E. THERMAL BLOOMING OVERVIEW**

The effects of a self-induced phase distortion and the resulting distortion of the laser beam irradiance that occur when a laser beam propagates through an absorbing medium like the atmosphere is termed "thermal blooming" [10]. The absorbed laser beam energy, normally a small fraction of the total laser beam energy, heats the medium, causing localized gradients in the density of the medium.

Consider a SFEL beam propagating through the atmosphere, having some absorption at the laser wavelength. If the atmosphere is in thermal equilibrium and the SFEL is turned on, the absorption will give rise to local heating which produces a small pressure increase. The affected atmosphere then expands at the speed of sound so as to restore the pressure balance. As the medium expands, the localized density will decrease with a corresponding drop in the local refractive index. If the cumulative effect of the negative refractive index change is large enough, it will result in a change in the shape of the laser beam profile. Since heating usually results in a decrease in refractive index of the medium in the center of the beam where the heating is greatest, the beam is usually defocused and spread. Thus, the beam grows in size or "blooms."

Gebhart [10] enumerates several factors that influence the impact thermal blooming has on a high energy laser beam. In general, these include:

1. the laser beam characteristics (i.e., wavelength, phase and irradiance distribution, and mode such as continuous wave, single pulse, or repetitively pulsed);

2. the kinetics of the absorption process, which determines the amount of time required for the absorbed energy to heat the atmosphere;
3. the mode of heat transfer that balances the absorbed energy ( i.e., thermal conduction, convection);
4. the propagation medium and scenario characteristics (i.e., path length, optical properties, platform speed, slewing, etc.).

As the beam passes through the atmosphere, there may be locations along its path which may allow the air around the beam to be stagnant relative to the beam. This "stagnation zone" will absorb energy from the beam and heat up. The heating of the air changes the index of refraction of the air. The energy crossing a unit area will be proportional to the square of the field. Since the field is usually stronger in the center of the beam, the air in the center of the stagnation zone will be heated more than the edges. The effect is to cause the portion of the beam passing through the center of the zone to propagate faster than at the edges. The zone acts as a diverging lens defocusing the beam.

As an example, consider a 1 liter (10 cm)<sup>3</sup> volume element of air with an extinction coefficient of 0.05/km. The fraction of absorbed power in the volume element is  $0.05/\text{km} \times 10\text{cm} = 5 \times 10^{-6}$ . Thus, if the laser provided 1 Megawatt, the absorbed power would be 5 Watts deposited in the 1 liter volume element of air. The specific heat of air is  $C_v = \Delta E / (V \Delta T) \approx 1 \text{ J/}^\circ\text{C}$ , where  $\Delta E$  is the amount of absorbed energy,  $V$  is the volume and  $\Delta T$  is the temperature rise. During a 1 second dwell time, the temperature rise in a 1 liter volume element would be  $5^\circ\text{C}$ . The length of a typical stagnation zone is 50m with the center of the laser beam passing through air that is  $5^\circ\text{C}$  hotter than the outside after a 1 second dwell time. The path length difference between the part of the beam that is hot and that which has not is calculated in the same way as (34). The region outside of the laser beam is not heated up and is traveling at the

propagation speed  $v$  in normal air, whereas, the inside of the laser beam is hot, has less air, and is traveling at speeds greater than  $v$ . Thus, the light inside the beam travels ahead of the light in the outer regions of the beam. Thermal blooming causes a phase difference between the inside and outside of the beam in proportion to the laser power  $|a|^2$ . The phase change is given by the following relation [3]:

$$d\phi_s = \Delta\phi_s |a(x,y)|^2 \quad . \quad (35)$$

The simulation program calculates the effect of the stagnation zone on the real and imaginary part of the laser field. Figure 7 results from a simulation of a stagnation zone at  $\tau = 0.6$  with an effective stagnation zone strength of  $\Delta\phi_s = 2$ . The stagnation zone strength  $\Delta\phi_s$  is defined similarly to the lens  $\Delta\phi$  of section C however, it is only applied to the stagnation zone. The effect of the zone is to cause the beam to defocus and is not random in Figure 7 because no turbulence is included. The field strength in the center of the beam decreases relative to the outer parts of the beam cross-section.

Figure 8 is the result of a beam propagating through an atmosphere consisting of  $ns = 100$  turbulent screens with a characteristic wavenumber,  $k_c = 4$ , and strength  $\Delta\phi_r = 600$ . The effect of the turbulence is to distort the shape of the beam and spread it over a larger area at the destination. This Figure combines the effect of turbulence and thermal blooming with  $\Delta\phi_s = 2$ . The distortion of the beam due to the turbulence is apparent as well as the defocusing effect of the stagnation zone. The result is less concentration of power at the desired point. Since blooming is affected by the field strength of the beam, increasing the power of the beam will only exacerbate the blooming effect. Therefore, the amount of power focused at the target will be less than expected and require a longer time for the beam to inflict the desired affect on the target.

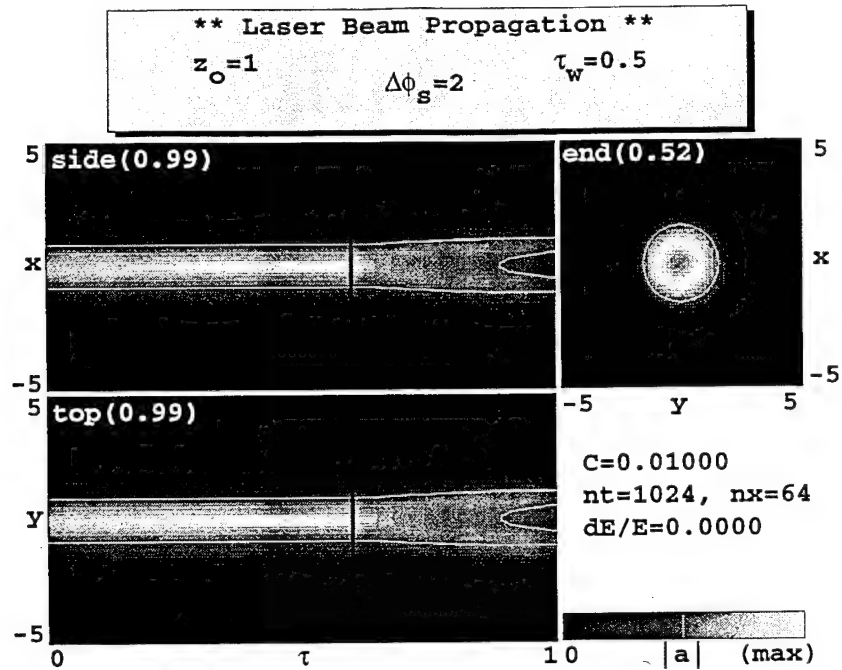


Figure 7. Propagation path through a stagnation zone.

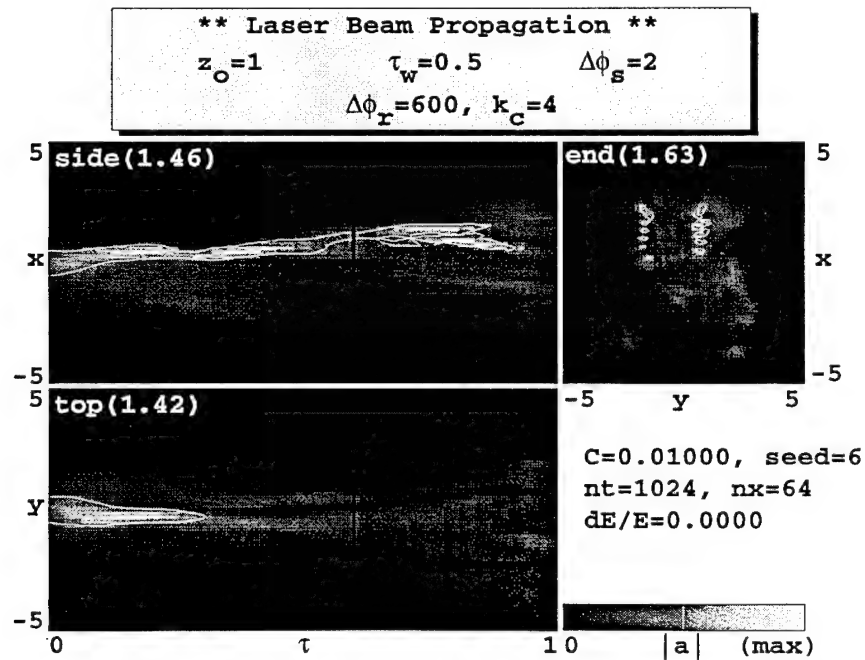


Figure 8. Propagation path through a stagnation zone and turbulence.

Although the non-linear blooming process can dominate the beam profile at high average power, linear interactions such as scattering and absorption combine to give an attenuation or extinction coefficient  $\alpha$  which decreases beam power [3][10]. Scattering due to aerosols such as smoke, mist, and suspended fine particles do not contribute to heating of the air in thermal blooming. The primary source of extinction is absorption. The absorption of power decays as  $P(z) = P_0 \exp(-\alpha z)$ . Where  $P_0$  is the original power level. Absorption, clearly the basis for thermal blooming, is very sensitive to wavelength. A SFEL allows wavelength tuning to avoid absorption while maintaining a narrow bandwidth. This provides a method of achieving peak beam irradiance at the target. The wavelength tunability of a SFEL is an important reason for selecting it over a conventional laser.



### III. BOEING 1 KILOWATT FEL

Boeing Corporation's Defense and Space Group has designed a visible-to-infrared wavelength FEL [13] capable of delivering 1 kw average optical power at  $\lambda = 0.6 \mu\text{m}$  wavelength. This high-average power FEL is driven by a 120 MeV linear accelerator (linac) generating 0.1 A average current in the macropulse with a 0.6% duty factor. The linac uses an 18 MeV, 433 MHz photo-injector, and a 1300 MHz longitudinal phase-space linearizer. The operational characteristics of the laser are presented in Table 1.

The first operational test of the laser is expected to be conducted in the visible wavelength region during fiscal year 1996. The laser and supporting laboratories are housed within a 40,000 square foot FEL research complex in Seattle, Washington [13]. This facility includes a 12 MW electric power substation, DC power vault, accelerator building with an upper radiation-shielded floor, and general purpose laboratory space. The electron beam parameter expectations described in Table 1 result from many experiments conducted over the past decade in support of the Department of Defense Strategic Defense Initiative and the French FEL program. The two cavity photo-injector has been operated at 25 percent duty factor and 32 mA average current [13]. This demonstrated capability is nearly 1000 times that performed by any other photo-injector. Additionally, test conducted in the 1980's at the  $0.6 \mu\text{m}$  wavelength indicate that the expected kilowatt class performance is feasible. An extraction efficiency of 1% with strong side-band generation was attained using a much more inefficient thermionic injector and three stage pulse compression [13].

Section IV highlights the theory of the FEL. In Section V, applications of the Boeing FEL will be examined with an emphasis on its military applications.

Parameter	Value
Energy KE	120 MeV
Peak Current $\hat{I}$	755 A
Undulator Periods $N$	220
Emittance $\varepsilon_n$ (4*rms)	$30\pi$ mm-mrad
Undulator Length $L$	5 m
Energy Spread $\delta\gamma/\gamma$	0.004
Undulator Parameter $\bar{K}$	1.31
Beam Radius $r_b$	0.016 cm
Mirror Separation $S$	20 m
Rayleigh Length $Z_0$	250 cm
Undulator Wavelength $\lambda_0$	2.18 cm
Wavelength $\lambda$	0.63 $\mu\text{m}$
Pulse Length $I_e$	7.0 ps/c
Quality Factor $Q$	90

Table 1. Characteristics of the Boeing 1 KW FEL [13].



#### IV. BASIC FEL THEORY

A FEL consists of three basic components: a relativistic electron beam, a static periodic magnetic field, and a co-propagating optical field [6]. A stream of relativistic electron bunches pass through an undulator which has a periodic magnetic field. Figure 9 is a simple schematic representation of a FEL and its basic components. As electrons sinusoidally traverse the undulator, they are accelerated resulting in radiation. Some of the spontaneous radiation may be stored in a laser resonator formed by placing two curved mirrors at the ends of the undulator. As the radiation builds up, the optical field in the undulator couples with the "wiggling" electron beam and results in stimulated emission and coherent radiation. The FEL can be described by classical electromagnetic theory. This results from a high density of photons within the optical wave [12].

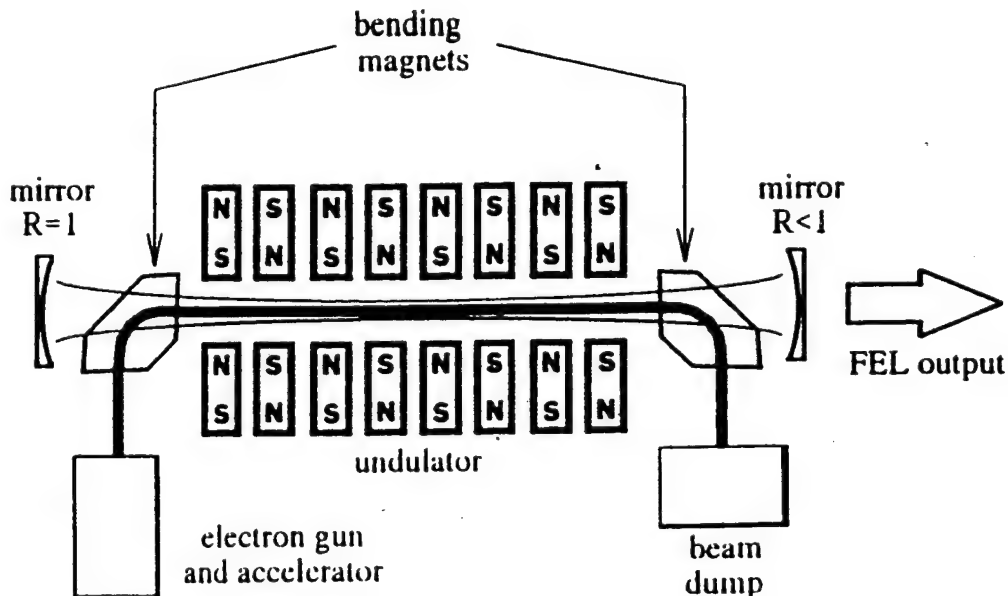


Figure 9. Schematic representation of the FEL. From Ref. [11].

## A. DIMENSIONLESS PARAMETERS

Recurring combinations of physical parameters in a FEL can be summarized by a few dimensionless parameters [6]. This discussion will enumerate many of the dimensionless variables and physical processes used throughout the following sections. Additional parameters will be explained as needed throughout section IV. For a detailed description of all FEL parameters see reference [6].

The undulator encompasses a series of magnets arranged to permit a periodic magnetic field along the longitudinal axis of the undulator. The dimensionless undulator parameter is  $K = e\bar{B}\lambda_0/(2\pi mc^2)$  where  $e$  is the electron charge magnitude,  $\bar{B}$  is the undulator root-mean-square (rms) magnetic field strength,  $\lambda_0$  is the undulator wavelength,  $m$  is the electron mass and  $c$  is the speed of light. The length of the undulator is  $L = N\lambda_0$ , where  $N$  is the number of magnetic field periods along the length of the undulator. The wiggling electrons interact with the optical field along the entire length of the undulator for a dimensionless duration of  $\tau = ct/L$  where  $\tau = 0 \rightarrow 1$ .

The relativistic electron energy is given by the Lorentz factor  $\gamma = E/(mc^2)$ . Here  $E$  is the beam energy and  $mc^2$  is the electron rest energy. The electron phase  $\zeta$  that characterizes the electron microscopic motion as they move down the undulator is

$$\zeta = (k + k_0)z(t) - \omega t \quad , \quad (36)$$

where the optical wavelength wave number is  $k = 2\pi/\lambda$ , the undulator wavelength wave number is  $k_0 = 2\pi/\lambda_0$ , the optical wavelength is  $\lambda$ , and the optical frequency is  $\omega = kc$ . The only dynamic variables in Equation (36) are the electron's longitudinal position  $z(t)$  and time  $t$ . In the relativistic limit,  $k \gg k_0$ , and the change in the electron phase is  $\Delta\zeta \approx k\Delta z$  where  $\Delta z$  is a spatial increment along the longitudinal axis in a section of the beam one

optical wavelength long. The electron phase velocity  $v(\tau)$  is the dimensionless time derivative of the electron phase as given by

$$v(\tau) \equiv \dot{\zeta}(\tau) = L[(k + k_0)\beta_z(t) - k] \quad . \quad (37)$$

Where the electron velocity in the  $z$  direction is given by  $c\beta_z$ . The optical and undulator field forces are resonant when  $v = 0$ . This yields the resonant optical wavelength condition which demonstrates the wavelength tunability of the FEL. Specifically, this relationship is given by:

$$\lambda = \lambda_0 \frac{[1 + K^2]}{2\gamma^2} \quad . \quad (38)$$

## B. ELECTRON TRAJECTORY

Electron trajectories in the undulator (wiggler) determine the character of the FEL interaction. It is the electron's "wiggling" motion in the undulator that provides coupling to the transverse optical field. A linear undulator, such as the "Thunder Wiggler" [13] used by Boeing's 1 kilowatt average power FEL, has a series of magnets along its length which provide a periodic magnetic field and generates linearly polarized light. Another type of wiggler is the helical undulator which uses coils of conducting wire wrapped around the beam line with current flowing in opposite directions in alternating turns [14]. This discussion will deal mainly with the linear undulator design.

A linearly-polarized magnetic field near the undulator axis  $\vec{B}_m$  [6] can be represented by

$$\vec{B}_m = B[0, \sin(k_0 z), 0] \quad , \quad (39)$$

where  $B$  is the magnitude of the undulator magnetic field, and  $k_0 = 2\pi/\lambda_0$  is the undulator wave number. The fields within a linearly polarized undulator in the vertical  $\hat{y}$  direction are illustrated in Figure 10. The forces acting on the

electrons within the undulator cavity are described by the Lorentz force equations:

$$\frac{d}{dt}(\gamma\vec{\beta}) = -\frac{e}{mc} \left[ \vec{E}_r + \vec{\beta} \times (\vec{B}_r + \vec{B}_m) \right] , \quad (40)$$

$$\frac{d\gamma}{dt} = -\frac{e}{mc} \left[ \vec{\beta} \cdot \vec{E}_r \right] , \quad (41)$$

$$\gamma = \frac{1}{\sqrt{1 - \vec{\beta} \cdot \vec{\beta}}} . \quad (42)$$

In the force equations,  $\vec{E}_r = E[\cos\Psi, 0, 0]$  is optical electric field,  $\vec{B}_r = E[0, \sin\Psi, 0]$  is the optical magnetic field,  $\Psi = kz - \omega t + \phi$  and  $c\vec{\beta}$  is the electron's velocity. Equation (40) represents conservation of momentum for the system and is commonly referred as the Lorentz force equation. Equation (41) describes the transfer of energy and (42) is the Lorentz factor. Since the forces exerted on an electron by the magnetic and electric components of the optical field nearly cancel each other, the net transverse optical force is significantly smaller than that of the transverse undulator magnetic field. Thus, the magnetic field in the undulator is the dominant field moving the electrons in the transverse direction. Substituting Equation (39) into (40), then integrating yields a perfectly sinusoidal beam trajectory in the xz plane as illustrated in Figure 10 and given by the following equation:

$$\vec{\beta}_\perp = -\frac{\sqrt{2}K}{\gamma} [\cos(k_0 z), 0, 0] . \quad (43)$$

In Equation (43),  $\vec{\beta}_\perp$  is the transverse component of the electron velocity. Assuming perfect injection into the undulator cavity makes the constant of integration zero. Similar approaches can be used to describe the motion of electrons in the helical undulator [6].

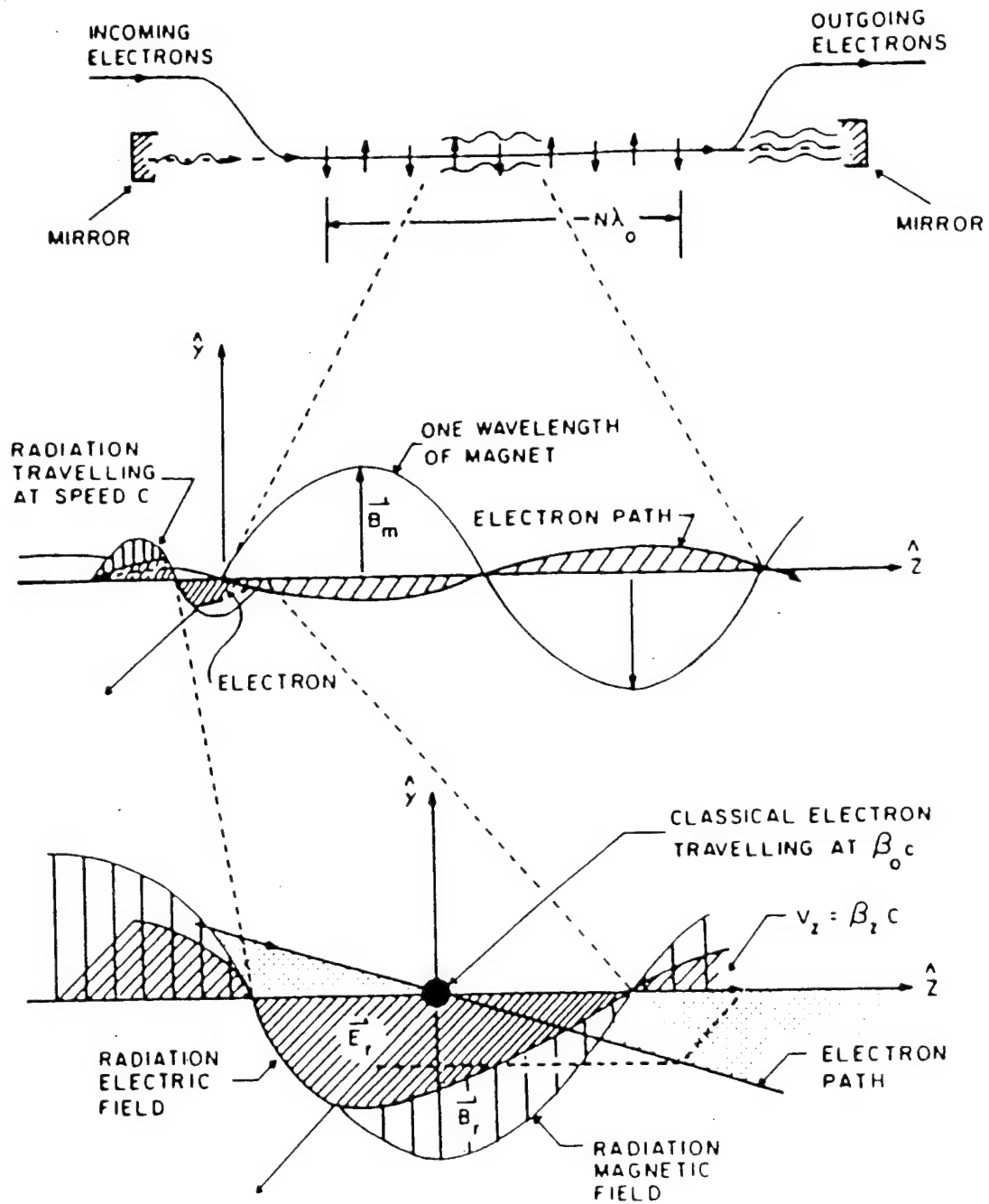


Figure 10. Fundamental physics of the FEL interaction. From Ref. [15].

### C. RESONANCE CONDITION

Accelerated electrons in the undulator of the FEL radiate energy. These electrons travel along the longitudinal axis of the undulator at relativistic speeds [6]. For the FEL to have gain, a net transfer of energy from the electron beam to the optical field must occur. This energy transfer is many orders of magnitude greater than the spontaneous emission contribution per pass [16]. Therefore, it is essential that stimulated emission occurs preferentially to stimulated absorption. For an optimum exchange of energy between an electron and the optical field, the electron must oscillate in phase with the optical field. This optimum energy exchange occurs when the electron falls behind the optical field by a distance of one optical wavelength within the span of one undulator period.

In a time interval  $\Delta t$ , the optical wave will travel a distance  $c\Delta t$  and the electron will travel a distance  $\beta_z c\Delta t$  where the axial component of the electron's velocity is represented by  $\beta_z$ . Take the interval  $\Delta t$  to be the time required for an electron to travel one undulator period or one wavelength. The light travels one wave length  $\lambda$  ahead of the slower electrons during time  $\Delta t$ , so that

$$\lambda = (c - \beta_z c) \frac{\lambda_0}{\beta_z c} \quad . \quad (44)$$

From reference [6] we know that  $\beta^2 = \beta_z^2 + \beta_\perp^2$  and recalling the Lorentz factor from Equation (42), the axial component of the electron velocity can be found. Thus, the axial component of the electron's velocity is

$$\beta_z = \left[ 1 - \beta_\perp^2 - \frac{1}{\gamma^2} \right]^{\frac{1}{2}} \quad . \quad (45)$$

Through a series expansion, Equation (45) can be approximated as

$$\beta_z \approx 1 - \frac{1 + \gamma^2 \beta_{\perp}^2}{2\gamma^2} \quad (46)$$

Squaring the magnitude of Equation (43) and substituting it into (46) gives

$$\beta_z = 1 - \frac{1 + K^2}{2\gamma^2} \quad (47)$$

Equation (47) relates the undulator parameter and the Lorentz factor to the axial component of the electron's velocity. From this simplification we can reduce Equation (44) into the resonance equation which is Equation (38). The resonance equation reveals the capacity of the FEL to be tunable. Since the wavelength of the optical field can be changed by adjusting the undulator parameter and/or the energy of the electron beam, the FEL can be continuously tuned to a desired wavelength within a prescribed bandwidth. This is a significant advantage over chemical lasers which are limited to a design wavelength.

#### D. PENDULUM EQUATION

This section reviews the motion of the electrons resulting from the interaction with the optical field. Electron dynamics in the FEL can be modeled by the pendulum equation [6]. The derivation of the pendulum equation begins by substituting  $\vec{E}_r$  from the previous section into (41). This yields

$$\dot{\gamma} = \frac{eKE}{\gamma mc} \cos(\zeta + \phi) \quad (48)$$

Two specific cases dealing with the argument of the cosine function in (48) are of interest. Firstly, when  $-\pi/2 < \zeta + \phi < \pi/2$  the cosine is positive and the electrons will gain energy from the optical field. In a similar fashion, when  $\pi/2 < \zeta + \phi < 3\pi/2$ , the cosine is negative and the electrons will lose energy to the optical field. Converting the time increment  $dt$  in (41) into a dimensionless time interval  $d\tau$  through  $dt = Ld\tau/c$ , Equation (41) becomes

$$\frac{d\gamma}{d\tau} = \frac{eKLE}{\gamma mc^2} \cos(\zeta + \phi) \quad . \quad (49)$$

Differentiating (47) with respect to  $\tau$  gives

$$\beta_z \dot{\beta}_z = \frac{(1 + K^2)\dot{\gamma}}{\gamma^3} \quad , \quad (50)$$

where the notation  $(\dot{\phantom{x}}) \equiv d(\phantom{x})/d\tau$ . Solving for  $\dot{\beta}_z$  and substituting in (49) gives

$$\dot{\beta}_z = \frac{(1 + K^2)eKLE}{\gamma^4 mc^2 \beta_z} \cos(\zeta + \phi) \quad . \quad (51)$$

Differentiating the electron phase velocity (37) with respect to  $\tau$  gives

$$\ddot{\zeta} = L(k + k_0)\dot{\beta}_z \quad . \quad (52)$$

Substituting the appropriate relations from the previous sections into Equation (52), and assuming  $k \gg k_0$ ,  $\beta_z \approx 1$ , and imposing the resonance condition [6] results in

$$\ddot{\zeta} = \frac{4\pi NeKLE}{\gamma^2 mc^2} \cos(\zeta + \phi) = |a| \cos(\zeta + \phi) \quad . \quad (53)$$

In the above equation, the dimensionless optical field strength is  $|a| = 4\pi NeKLE/\gamma^2 mc^2$ . Equation (53) is the electron pendulum equation which governs the electron's phase-space motion within the undulator and under the influence of the optical wave [6].

## E. OPTICAL WAVE EQUATION

By adding a current density to the homogeneous complex optical wave equation described in Section IIB, the complex optical wave Equation (1) can be rewritten as [6]

$$\left[ \nabla^2 - \frac{1}{c^2} \frac{\partial^2}{\partial t^2} \right] \vec{A}(\vec{r}, t) = -\frac{4\pi}{c} \vec{J}_\perp \quad . \quad (54)$$

In the above expression the transverse electron beam current is  $\vec{J}_\perp$ . Following



the arguments presented in Section IIB and substituting Equation (4) into (54) yields

$$\frac{\partial E}{\partial t} = -2\pi \vec{J}_\perp \cdot \hat{\epsilon}_1, \quad (55)$$

and

$$E \frac{\partial \phi}{\partial t} = 2\pi \vec{J}_\perp \cdot \hat{\epsilon}_2. \quad (56)$$

Here  $\hat{\epsilon}_1 = [\cos\Psi, -\sin\Psi, 0]$  and  $\hat{\epsilon}_2 = [\sin\Psi, \cos\Psi, 0]$  are orthogonal unit vectors.

The transverse electron beam current is the sum of the contributions of each individual electron [6]. Thus, each electron contributes

$$\vec{J}_{\perp i} = -ec\vec{\beta}_\perp \delta^{(3)}(\vec{x} - \vec{r}_i), \quad (57)$$

where  $\vec{r}_i$  is the position of the  $i$ th electron and  $\delta^{(3)}(\dots)$  is the three dimensional Dirac-delta function [6]. Taking the dot product of (57) with the unit vectors yields

$$\vec{J}_{\perp i} \cdot \hat{\epsilon}_{[1]} = \frac{eKc}{\gamma} \begin{bmatrix} \cos(\zeta + \phi) \\ \sin(\zeta + \phi) \end{bmatrix} \delta^{(3)}(\vec{x} - \vec{r}_i). \quad (58)$$

Assuming a constant electron density  $\rho$  and summing over all sample electrons, the electric field can be written as

$$\dot{E} = -2\pi eKc\rho \left\langle \frac{\cos(\zeta + \phi)}{\gamma} \right\rangle, \quad (59)$$

$$E\dot{\phi} = 2\pi eKc\rho \left\langle \frac{\sin(\zeta + \phi)}{\gamma} \right\rangle, \quad (60)$$

which indicates that if  $\dot{E} > 0$ , the laser beam energy grows. Specifically, this will happen if  $(\zeta + \phi) \approx \pi$ . Given a dimensionless beam current [6] of  $j = 8N(e\pi KL)^2\rho/(\gamma^3 mc^2)$ , and the dimensionless optical wave amplitude  $|a|$  from Section IVD, Equations (59) and (60) will yield

$$\dot{|a|} = -j \langle \cos(\zeta + \phi) \rangle, \quad (61)$$

and

$$\dot{\phi} = \frac{j}{|a|} \langle \sin(\zeta + \phi) \rangle \quad (62)$$

Equations (61) and (62) may be combined to yield

$$\dot{a} = -j \langle e^{-i\zeta} \rangle \quad (63)$$

Where  $a = |a| e^{i\phi}$ . Equation (62) reveals that an increase in the optical field strength will result in a decrease in the optical phase evolution rate, while an increase in the dimensionless electron beam current will result in an increase of the optical field phase evolution rate. Moreover, in the absence of current,  $j = 0$ , the FEL optical wave envelope does not evolve. Similarly, when there is current, but no bunching, and thus  $\langle \dots \rangle = 0$ , there is also no change in the optical field [6].

## F. TRAPPED-PARTICLE INSTABILITY

At the onset of strong-field saturation, the electrons in the beam tend to travel in closed phase-space orbits resulting in increased FEL efficiency. During this interaction some of the electrons will overtake other electrons in the beam. This results in diminished bunching and gain. A direct consequence of this is that some electrons will become trapped in deep potential wells in phase-space. This phenomena is termed the "trapped-particle instability." It is exhibited when either the FEL amplifier or oscillator evolve to power levels beyond the onset of saturation. Figure 11 depicts a group of electrons traveling through one pass of the undulator and becoming trapped in the potential well of phase-space.

The pendulum equation (53) can be expanded about the stable fixed-point [6]  $\zeta = \pi/2$ , so that  $\zeta = \pi/2 + x$ , where the spatial increment  $x \ll \pi$ . A solution describing the motion of the trapped electrons is

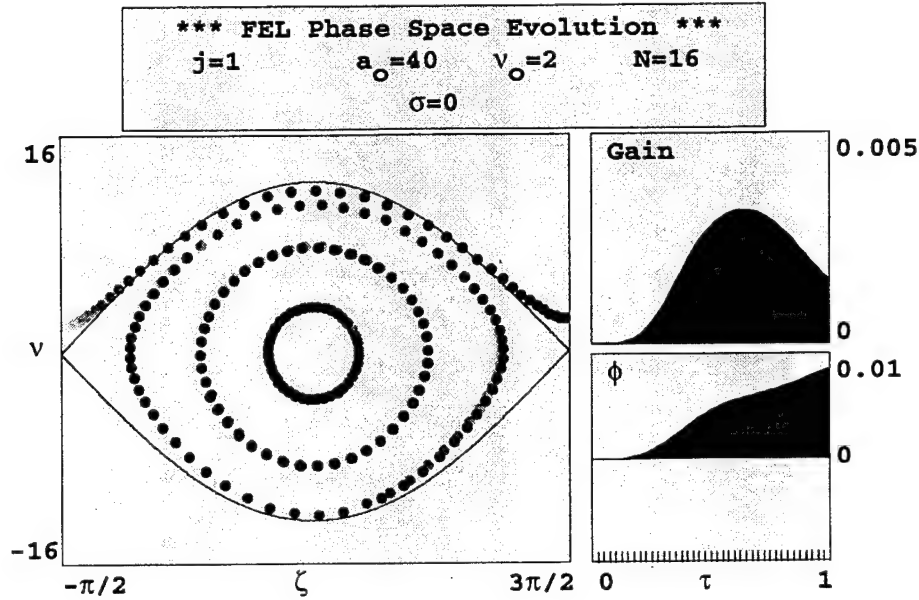


Figure 11. Phase-space evolution showing trapped-particle instability in an untapered undulator.

$$\zeta(\tau) \approx \zeta_0 + \frac{v_0}{v_s} \sin(v_s \tau) \quad , \quad (64)$$

where  $v_s = \sqrt{|a|}$  is the "synchrotron" or the "trapped-particle" frequency. Under certain conditions, this will produce sidebands in the optical power with frequency  $\nu = \nu_0 \pm \nu_s$  and wavelengths shifted away from the fundamental by  $\Delta\lambda/\lambda = \nu_s/(2\pi N)$  [6].

The interaction of electrons along the length of the undulator can be altered by modifying the properties of the undulator. Tapering the undulator will alter the gain spectrum and the electron beam interaction [6], giving the FEL increased power at saturation. At normal saturation, electrons lose sufficient energy to enable them to drop out of the gain spectrum bandwidth. As the energy of the beam decreases and shifts across the gain bandwidth, the

resulting change in the beam's phase velocity is given by  $\Delta v \approx 4\pi N \Delta\gamma/\gamma \approx -2\pi$ , where  $\Delta\gamma/\gamma$  is the change in the beam's energy. A resonant interaction can be re-established by tapering the undulator field in order to extract more energy from the trapped electrons. When operating properly, the FEL reaches high-power saturation and about half the electrons are trapped in the closed orbits of phase-space.

The dimensionless synchrotron frequency for the trapped electrons in a tapered undulator is  $\nu_s \approx (|a|^2 - \delta^2)^{1/4}$  where  $|a|$  is the dimensionless optical field strength, and  $\delta$  is the phase acceleration in the pendulum equation [6],

$$\ddot{\zeta} = |a| \cos(\zeta + \phi) \quad . \quad (65)$$

This equation shows that  $|a|$  must be greater than  $\delta$  in order to trap electrons [6]. In an untapered undulator  $\nu_s = \sqrt{|a|}$ . Comparing Figures 11 and 12, it is apparent in Figure 12, that roughly half of the electrons are trapped in the potential well with a taper  $\delta = 4\pi$ . Figure 12 illustrates the final position of the electrons in the separatrix.

The onset of the trapped-particle instability can be seen in Figure 11. For a full synchrotron oscillation, the optical field strength is  $|a| = 4\pi^2 \approx 40$  [6], which corresponds to a separatrix height of  $4|a|^{1/2} \approx 25$  [6]. This causes the electrons to travel in a closed orbit about the fixed point  $(\zeta, \nu) = (\pi/2, 0)$  in phase space [6].

## G. DESYNCHRONISM OVERVIEW

This section only presents the rudimentary principles of desynchronization  $d$  [6]. When both the electron and the optical pulse enter the undulator simultaneously they are said to be synchronized when  $d = 0$ . The leading edge of the optical pulse immediately commences overtaking the electron pulse. In weak fields, the optical wave experiences no gain at the beginning of the

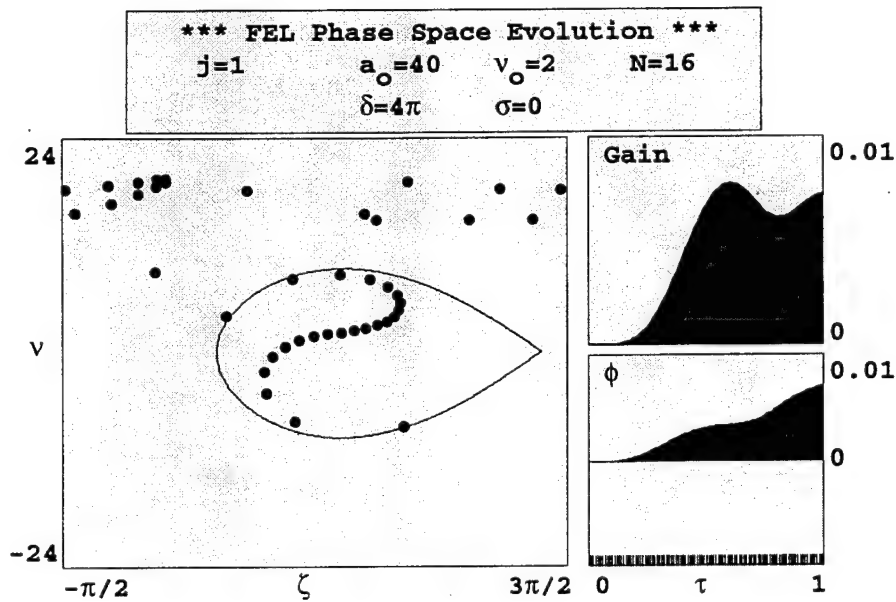


Figure 12. Phase-space evolution showing trapped-particle instability in a tapered undulator.

undulator and the electron bunching is slow to occur. This delay in the electron-optical gain mechanism is known as lethargy [6]. The initial part of the optical pulse is poorly coupled to the electron beam and decays. As time progresses, the increased gain and corresponding bunching of electrons provides the necessary interaction for field coupling. This causes the trailing edge of the optical pulse to grow, thereby, distorting the optical pulse. The distortion of the optical pulse continues on every subsequent pass through the undulator as gain is preferentially deposited on the trailing edge of the pulse [6]. Essentially, the centroid of the light pulse travels slightly slower than  $c$ . Over many passes through the undulator, gain continues to grow on the trailing edge of the optical pulse resulting in eventual power decay. This occurs when the optical pulse centroid moves away from the electron pulse, and the optical

wavefront is no longer driven by bunched electrons. Under this condition the steady-state power goes to zero [16].

Near  $d \approx 0$ , short pulse effects restrict coupling and the steady-state power is zero. Slightly increasing desynchronism leads to a sharp rise in optical power, where the electron and optical pulse repetition rates are most nearly matched. Under this condition the FEL could become subject to the trapped-particle instability. Increasing  $d$  further causes the electron and optical pulses to stop overlapping over many passes through the undulator. Thus, the interaction of the electrons with the optical beam deteriorates resulting in decreased power and gain [6]. In summary, too much or too little desynchronism is detrimental to FEL power and gain.

## V. APPLICATION OF BOEING FEL

Applications of the Boeing 1KW FEL can be categorized into three groups: industrial, research, and defense. Industrial applications include commercial isotope production and pharmaceutical material processing. Research opportunities are far ranging and include cancer treatment and semiconductor development. Defense application include both shipboard defensive and offensive weapon systems. This discussion will be limited to the use of the Boeing FEL as an Anti-Ship Missile Defense (ASMD) system.

As a defensive system, the FEL is an excellent ASMD weapon as argued in Section I. Assuming Boeing will achieve its ambitious objectives, the next concern is the quality of the optical beam exiting the FEL. Boeing's high average power FEL is expected to yield 1kw average optical power at  $\lambda = 0.6 \mu\text{m}$  wavelength. This section will focus on applying the principles presented in Sections II, IV to determine if the necessary beam quality can be achieved. The focus will be on the trapped-particle instability and ways of minimizing its effect in the Boeing FEL. Boeing's plan is to eliminate the instability in order to narrow the power spectrum for better propagation through a transmissive window in the atmosphere.

Figure 13 illustrates the trapped-particle instability in an untapered undulator with dimensionless parameters corresponding to the values of Table 1. The dimensionless current density  $j = 658$  is derived from the average current [13]. The parameters  $a_0$  and  $v_0$  are the dimensionless optical field, and electron phase velocity, respectively. Lastly,  $\sigma_G$  is the induced phase velocity spread. In the figure, it is evident that most of the particles are trapped inside the separatrix. Thus, the necessary interaction between the optical field and the electron beam is not taking place. In fact, the electrons are absorbing

energy from the optical field. The peak-to-peak separatrix height is  $4\sqrt{a} \approx 4v_s = 4\sqrt{5000} \approx 280$ . Additionally, the synchrotron oscillation frequency is  $v_s \approx \sqrt{a} \approx 70$  giving  $v_s/2\pi \approx 11$  synchrotron oscillations along the undulator length as shown in Figure 13. Oscillations in the evolution of the gain  $G(\tau)$  and the optical phase  $\phi(\tau)$  are illustrated at the right side of the figure and are caused by the oscillations of the electron bunch in the harmonic closed orbits around the stable fixed point inside the separatrix.

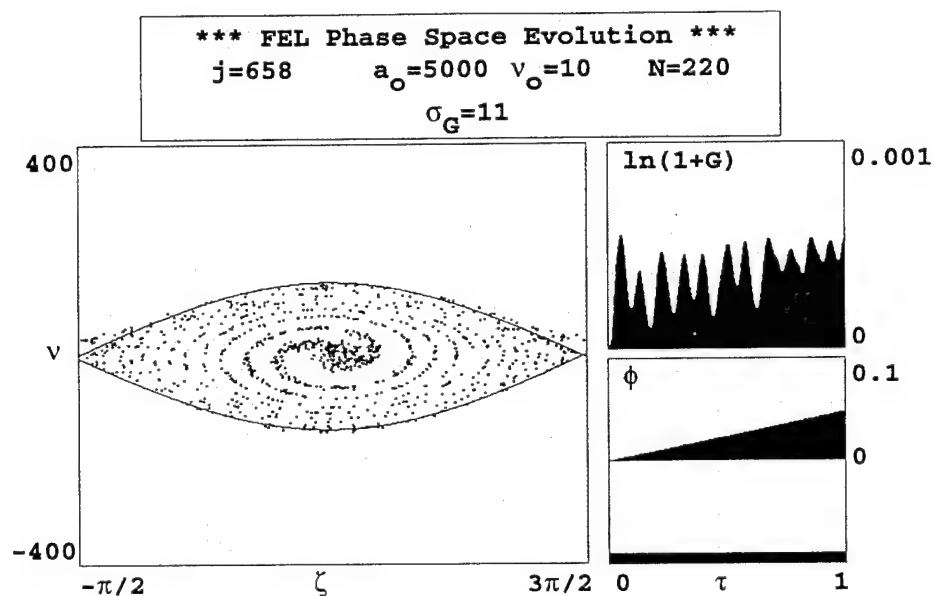


Figure 13. Phase-space evolution showing trapped-particle instability in an untapered undulator.

Figure 14 incorporates a 10% energy taper represented by  $\delta = 4\pi N\Delta\gamma/\gamma \approx 88\pi$  [13]. The energy taper dramatically reduces the synchrotron oscillations and results in roughly a 4% increase in gain. Additionally, approximately half of the electrons are trapped in the potential well. These simulations indicate the chosen energy taper may reduce the trapped-particle



instability. However, these simulations only model one pass through the undulator. Modeling over many passes through the undulator is necessary to describe the performance of the tapered undulator.

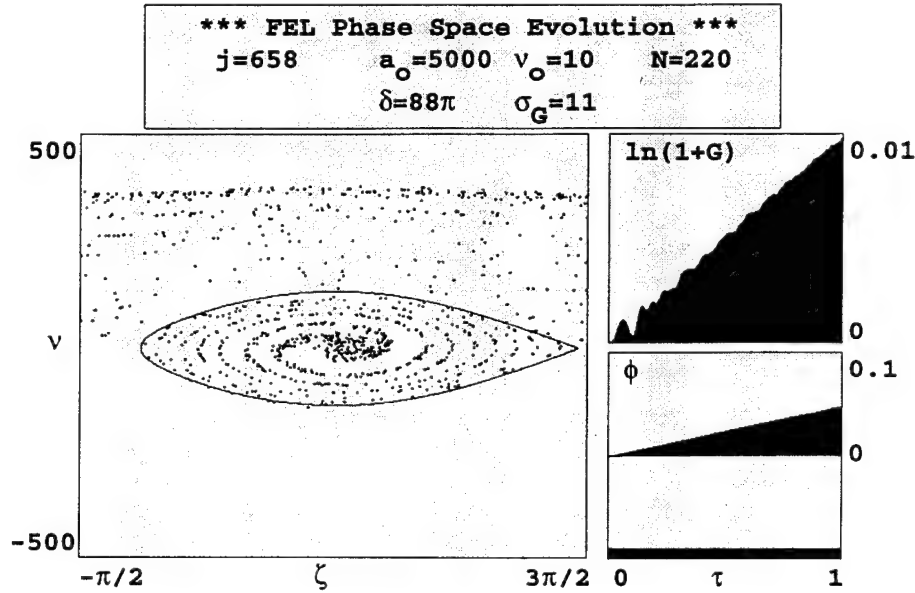


Figure 14. Phase-space evolution showing trapped-particle instability in a tapered undulator.

In both the tapered and untapered cases, sidebands can form around the fundamental frequency at  $v_0 \pm n v_s$ . Figure 15 illustrates the results of a simulation with periodic boundary conditions in a window corresponding to one slippage distance along the beam. The dimensionless current is  $j = 658$  at all points in the window, and interacts with the optical field for  $n = 400$  passes. The electrons start uniformly spread in phase along  $z$  with a phase velocity spread of  $\sigma_G = 11$ . The resonator loss on each pass is determined by  $Q = 5$  corresponding to 20% loss [13].

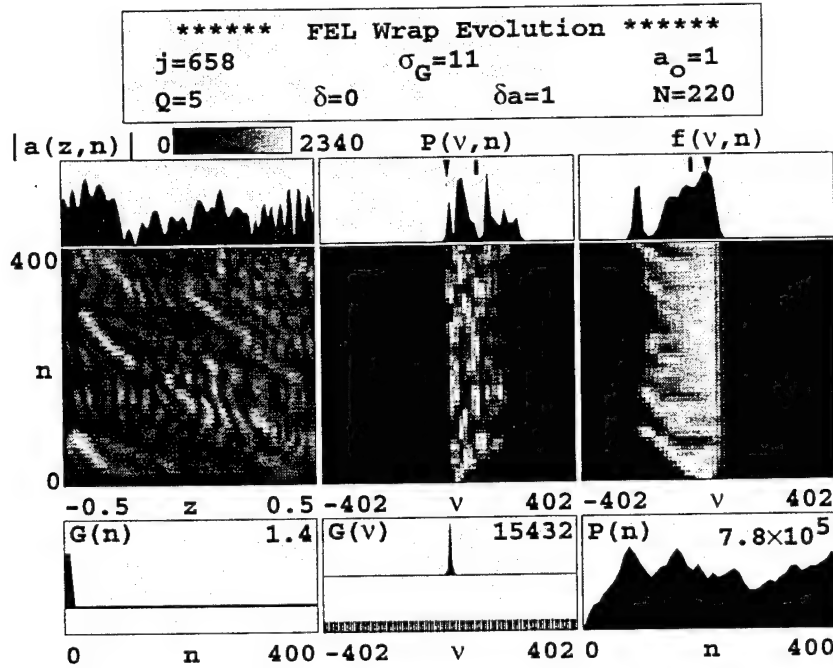


Figure 15. FEL Wrap Evolution with an untapered undulator.

The bottom-left corner of Figure 15 shows the gain,  $G(n)$ , at the end of each pass through the undulator, starting at resonance  $v_0 = 0$  from initial optical field  $a_0 = 1$ , with noise  $\delta a = 1$ . Other modes begin to grow increasing the gain and the power  $P(n)$  shown at the bottom right. As the electrons slip back past an optical field site executing synchrotron oscillations, they continually modulate the wave envelope. The middle-left box depicts a chaotic optical field amplitude after mode saturation and the growth of sidebands. The peak field amplitude is  $|a(z,n)| \approx 2340$ . The middle-center plot shows the optical power spectrum  $P(v,n)$ . Power  $P(n)$  increases dramatically as sidebands appear in the power spectrum  $P(v,n)$ . The final power spectrum  $P(v)$  shows several prominent sidebands up to  $\delta v \approx 200$  away from the fundamental. The frequency spread is large at  $\Delta\lambda/\lambda \approx \delta v/2\pi N \approx 15\%$  with a 7% shift away from resonance. The rectangular tick mark points at the center of the final power spectrum.

The electron phase velocity spectrum  $f(v,n)$  at the top-right corner of Figure 15 shows how a spread is caused by the trapping of electrons in strong optical fields. The rectangular tick-mark indicates the final value of the beam's averaged phase-velocities and shows a loss of energy corresponding to  $\Delta\gamma/\gamma \approx \langle\Delta v\rangle/4\pi N \approx 2\%$  with a large spread of more than 8%. The spread in the electron's phase-velocity distribution at the end of each pass  $f(v,n)$ , increases as the strong optical fields extract more energy from the beam. The peak-to-peak height of the closed-orbit region of phase space,  $4\sqrt{|a|} \approx 4v_s$ , gives an estimate of the induced spread at each pass. In normal, single mode saturation the electron spread is only  $v_s \approx 2\pi$ , after the trapped-particle instability occurs, the peak field is,  $|a| \approx 2340$  increasing the synchrotron frequency to  $v_s \approx 15\pi$ .

Figure 16 is a simulation conducted with the same parameters as Figure 15, but with the addition of a 10% energy taper in the undulator of  $\delta = 88\pi$  and increased  $Q = 10$  [13,6]. The sidebands are not eliminated. Both the sidebands and the trapped-particle instability occur causing the peak field amplitude to be chaotic and destroying the operation of the tapered undulator. The average wavelength shift is  $\delta\lambda/\lambda \approx 4\%$  with a wavelength spread of  $\approx 8\%$ . The electron beam energy spread is greater than 10% due to the large taper, but most electrons remain untrapped. We tried simulations starting with much stronger optical fields, and with a smaller 5% taper ( $\delta = 44\pi$ ), but could not find parameters that would allow a single-mode optical field so that the tapered undulator could work properly.

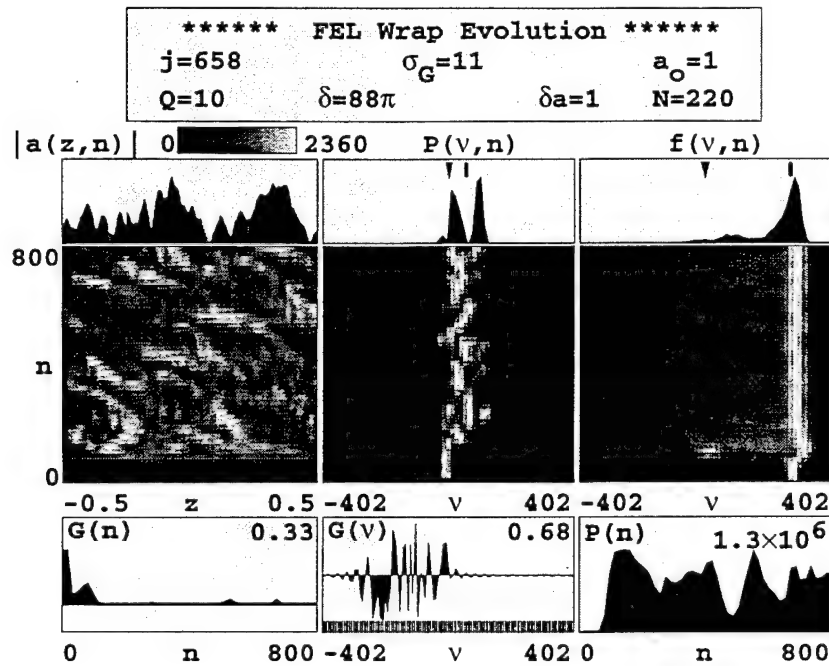


Figure 16. FEL Wrap Evolution with a tapered undulator.

## VI. CONCLUSION

The development of a high average power FEL for military applications, whether shipboard or not, represents a significant advancement in technology over present weapon systems design. The FEL has significant advantages over conventional kinetic systems and other classical high-energy laser systems. The rapid response, wavelength tunability, and infinite magazine make the FEL a highly desirable shipboard weapon system.

The proposed Boeing 1kw FEL will demonstrate the highest average power attained to date in an FEL. The supporting experiments over the past decade validate their high expectations of achieving high-average power. The simulations of Section II indicate the need to have a narrow bandwidth spectrum to enable propagation through a turbulent atmosphere and overcome the affects of thermal blooming. By tuning the wavelength of the FEL these atmospheric losses can be overcome and the desired energy can be deposited on target. The simulations of Section V indicate that the Boeing design has potential; however, Boeing must correct its wide bandwidth problem.



## LIST OF REFERENCES

1. Jane E. Nolan and Albert D. Wheelon, "Third World Ballistic Missiles", Scientific American, v. 263, No. 2, August 1990.
2. N. Friedman, The Naval Institute Guide to World Naval Weapon Systems, Naval Institute Press, Annapolis, Maryland, pp.81-82, 1989.
3. Prof W. B. Colson, PH4911 COURSE: Simulation of Physical and Weapon Systems, Naval Postgraduate School, Monterey, CA.
4. S. F. Clifford, "The Classical Theory of Wave Propagation in a Turbulent Medium," Topics in Applied Physics, v. 25, July, 1978.
5. J. R. Reitz, F. J. Milford, R. W. Christy, Foundations of Electromagnetic Theory, 4th ed., Addison-Wesley Publishing Company, New York, 386-408, 1992.
6. W. B. Colson, "Classical Free Electron Laser Theory," Laser Handbook, W. B. Colson, C. Pellegrini, and A. Renieri (eds.). North-Holland Physics, Elsevier Science Publishing Co. Inc., The Netherlands, 1990.
7. C. B. Hogge, "Propagation of High Energy Laser Beams in the Atmosphere," High Energy Lasers and Their Applications, v.1, Addison-Wesley Publishing Company, Reading, Massachusetts, 177-247, 1974.
8. E. C. Crittenden, Jr., A. W. Cooper, E. A. Milne, G. W. Rodenback, S. H. Kalmbach, "Effects of Turbulence on Imaging Through the Atmosphere," SPIE Symposium on Optical Properties of the Atmosphere, Washington, DC, 30-31 March 1978.
9. F. G. Gebhart, "High Power Laser Propagation," Applied Optics, v. 15, No. 6, June 1976.
10. F. G. Gebhart, "Nonlinear Propagation: Thermal Blooming," IR/EO Systems Handbook, Atmospheric Propagation of Radiation, v. 2, SPIE Optical Engineering Press, Bellingham, Washington, 1993.

11. W. R. Pinkley, "Wavelength Modulation In Free Electron Lasers," Master's Thesis, Naval Postgraduate School, March 1995.
12. J. B. Murphy and C. Pellegrini, "Introduction to the Physics of the FEL," Laser Handbook, W. B. Colson, C. Pellegrini, and A. Renieri (eds.). North-Holland Physics, Elsevier Science Publishing Co. Inc., The Netherlands, 1990.
13. J. Adamski, D. Dowell, C. Parazzoli, and A. Vetter, WHITE PAPER: A High Average Power Free Electron Laser User Facility for Defense and Civilian Applications, March 1995.
14. D. D. Quick, "Simulations of the High Average Power SELENE Free Electron Laser Prototype," Master's Thesis, Naval Postgraduate School, June 1994.
15. W. F. Wilkenson, "A Theory for Optical Wavelength Control in Short Pulse Free Electron Laser Oscillators," Master's Thesis, Naval Postgraduate School, June 1993.
16. Prof W. B. Colson, PH4998 COURSE: Advanced FEL Theory Seminar, Naval Postgraduate School, Monterey, CA.



## INITIAL DISTRIBUTION LIST

- |    |  |   |
|----|--|---|
| 1. | Defense Technical Information Center     | 2 |
|    | 8725 John J. Kingman Rd., STE 0944       |   |
|    | Ft. Belvoir, Virginia 22060-6218         |   |
| 2. | Library, Code 13                         | 2 |
|    | Naval Postgraduate School                |   |
|    | Monterey, California 93943-5002          |   |
| 3. | Professor William B. Colson, Code PH/Cw  | 9 |
|    | Department of Physics                    |   |
|    | Naval Postgraduate School                |   |
|    | Monterey, California 93943-5000          |   |
| 4. | Professor Robert L. Armstead, Code PH/Ar | 1 |
|    | Department of Physics                    |   |
|    | Naval Postgraduate School                |   |
|    | Monterey, California 93943-5000          |   |
| 5. | Lieutenant Luis Ramos                    | 2 |
|    | 2501 Alleghany Loop                      |   |
|    | Virginia Beach, VA 23456                 |   |
| 6. | Thomas Felder                            | 1 |
|    | 17413 Hawthorne DR.                      |   |
|    | Lowell, IN 46356                         |   |